

PAPER • OPEN ACCESS

## Complex electrical spiking activity in resistive switching nanostructured Au two-terminal devices

To cite this article: M Mirigliano *et al* 2020 *Nanotechnology* **31** 234001

View the [article online](#) for updates and enhancements.

### Recent citations

- [Enhancing composition control of alloy nanoparticles from gas aggregation source by in operando optical emission spectroscopy](#)  
Jonas Drewes *et al*
- [Anomalous electrical conduction and negative temperature coefficient of resistance in nanostructured gold resistive switching films](#)  
M. Mirigliano *et al*
- [Dynamic Electrical Pathway Tuning in Neuromorphic Nanowire Networks](#)  
Qiao Li *et al*





**IOP | ebooks™**

Bringing together innovative digital publishing with leading authors from the global scientific community.

Start exploring the collection—download the first chapter of every title for free.

# Complex electrical spiking activity in resistive switching nanostructured Au two-terminal devices

M Mirigliano<sup>1</sup>, D Decastri<sup>1</sup>, A Pullia<sup>1</sup>, D Dellasega<sup>2</sup>, A Casu<sup>3</sup>, A Falqui<sup>3</sup>  and P Milani<sup>1</sup> 

<sup>1</sup> CIMAINA and Department of Physics, Università degli Studi di Milano, via Celoria 16, I-20133, Milano, Italy

<sup>2</sup> Department of Energy, Politecnico di Milano, via Ponzio 34/3, I-20133, Milano, Italy

<sup>3</sup> King Abdullah University of Science and Technology (KAUST), Biological and Environmental Sciences and Engineering (BESE) Division, NABLA Lab, 23955-6900 Thuwal, Saudi Arabia

E-mail: [paolo.milani@mi.infn.it](mailto:paolo.milani@mi.infn.it)

Received 16 October 2019, revised 30 January 2020

Accepted for publication 17 February 2020

Published 23 March 2020



CrossMark

## Abstract

Networks of nanoscale objects are the subject of increasing interest as resistive switching systems for the fabrication of neuromorphic computing architectures. Nanostructured films of bare gold clusters produced in gas phase with thickness well beyond the electrical percolation threshold, show a non-ohmic electrical behavior and resistive switching, resulting in groups of current spikes with irregular temporal organization. Here we report the systematic characterization of the temporal correlations between single spikes and spiking rate power spectrum of nanostructured Au two-terminal devices consisting of a cluster-assembled film deposited between two planar electrodes. By varying the nanostructured film thickness we fabricated two different classes of devices with high and low initial resistance respectively. We show that the switching dynamics can be described by a power law distribution in low resistance devices whereas a bi-exponential behavior is observed in the high resistance ones. The measured resistance of cluster-assembled films shows a  $1/f^\alpha$  scaling behavior in the range of analyzed frequencies. Our results suggest the possibility of using cluster-assembled Au films as components for neuromorphic systems where a certain degree of stochasticity is required.

Keywords: resistive switching, neuromorphic devices, cluster-assembled films

(Some figures may appear in colour only in the online journal)

## 1. Introduction

Significant performance improvements of computational systems based on von Neumann architecture, in terms of data handling and processing, are hardly sustainable at extreme miniaturization due to the required energy dissipation capabilities [1–4]. An approach aiming at the reproduction of the

human brain architectural and dynamical properties has been proposed to overcome these limitations [3, 5].

Neurons and synapses are the two basic computational units in the brain: a neuron receives the inputs coming from other neurons and, on the basis of its own kind of activation function, can in turn generate electrical spikes as an output [6]. Synapses are the further key factor for the overall computation capability of a neuronal system [6, 7]. The synaptic strength between neurons, i.e. of their connections, is modified by both repeated and/or modified neural activity both in pre-synaptic and post-synaptic cells (Hebb's postulate) [6]. Furthermore, in the late 1990s, spike-timing-dependent



Original content from this work may be used under the terms of the [Creative Commons Attribution 4.0 licence](https://creativecommons.org/licenses/by/4.0/). Any further distribution of this work must maintain attribution to the author(s) and the title of the work, journal citation and DOI.

plasticity (STDP), based on the temporal order of spikes, emerged as a form of Hebbian learning [7].

The spontaneous firing of spikes from a network of neurons displays spatial and temporal correlation [8, 9] and it is expected to have a major neurobiological function [10–13]. Neuronal networks also display irregular spontaneous activity characterized by intermittent bursts separated by periods of reduced activity. Long-range correlations of the irregular spontaneous activity have been extensively studied *in vitro* showing power law dynamics and long-range interactions [11–13].

The inter-spike intervals (ISI) of the spontaneous firing of neuronal networks show different distributions [8], *in vitro* hippocampal neuronal networks show a spontaneous spiking activity with temporal correlation on a time scale of hundreds of milliseconds. The power spectrum of the network firing rate as function of the frequency showed significant  $1/f$  trend below 1 Hz [8].

Noise in neural systems is of fundamental importance for information processing in nonlinear systems [14–16]. The development of neuromorphic hardware containing probabilistic spiking units aims at the reproduction of the stochastic behavior present in biological neuronal networks [14, 17, 18].

The fabrication of artificial hardware mimicking aspects of the spiking activity of biological systems is difficult to achieve with top-down CMOS-based technologies [19]. To date, artificial realization of neuromorphic architectures has been limited by the capacity to fabricate robust interconnects between electronic components in a cost-efficient manner, especially in designs utilizing unconventional topologies [1, 2, 17, 19].

Networks based on the bottom-up assembling of nanoscale building blocks and showing resistive switching activities are becoming increasingly popular as possible solutions for a straightforward fabrication of complex architectures with neuromorphic features [20–23]. The electrical activity of random resistive switch networks does not rely on the integration of specific devices, but is encoded in the collective nonlinear dynamic switching behavior as a result of an applied input signal [21]. There has been an increasing number of reports on resistive switching observed in nanoparticle assemblies [20, 24–26] and on various proposed mechanisms for such behavior in both uniform [24] and non-uniform thin films and nanocomposites [20].

In nanoparticle assemblies the observation of resistive switching has been attributed to filament formation between individual metal particles likely due to charge carrier migration across undoped regions with a moving boundary [22, 27] or attractive van der Waals forces [20]. In many cases the nanoparticles were coated with an organic molecule, oxide or polymer layer through which resistive switching occurs via redox activity, the formation of a charge-transfer complex, or the formation of donor–acceptor couples [22, 28–30].

Recently we have showed that metallic nanostructured Au films fabricated by bare gold nanoparticles, produced in the gas phase, and with thickness well beyond the electrical percolation threshold, show a non-ohmic electrical behavior

and complex and reproducible resistive switching [21]. Here we quantitatively analyze the electrical spiking activity of nanostructured Au two-terminal devices in terms of ISI and power spectral density (PSD) in order to assess the characteristics potentially interesting for neuromorphic data handling [8, 31].

## 2. Experimental methods

### 2.1. Device fabrication

Two-terminal devices based on nanostructured Au films were fabricated by Supersonic Cluster Beam Deposition [32]: the deposition apparatus is equipped with a Pulsed Microplasma Cluster Source (PMCS) that allows the production of neutral clusters in gas phase as described in details in [33]. Briefly, the PMCS principle of operation consists on the ablation of a gold rod by a plasma ignited during the injection of a high-pressure pulse of argon. The species resulting from the target ablation condense through collision with the Argon gas forming Au clusters, then the cluster-gas mixture is expanded through a nozzle forming a supersonic seeded beam [32]. The cluster beam is then focused by an aerodynamic lenses system [34] and directed on silicon substrates where a silicon oxide layer has been previously formed by thermal annealing. In figure 1 the scheme of the experimental apparatus is shown.

The substrates are mounted on a holder to allow the *in situ* characterization of the evolution of the electrical resistance of the cluster-assembled film during the deposition. A quartz microbalance (not shown in figure 1), positioned near the samples, periodically monitors the amount and the rate of deposited material and it allows to make an estimation of the nominal thickness of the films. This configuration allows the parallel production of different devices characterized by different nanostructured film thickness and hence initial electrical resistance [24].

In figure 1 (bottom right) we show a schematic representation of the two-terminal device: the cluster assembled film is deposited, by using a stencil mask, in the gap between two gold electrodes previously fabricated by thermal evaporation as described in detail in [24].

We fabricated two classes of devices using films with thickness in different regions of the percolation curve and hence different initial resistances: high initial resistance (HIR) in the range  $10^4 < R < 10^5 \Omega$  (thickness 10–15 nm, in the nonlinear region of percolation curve, where a large resistance decreasing corresponds to a narrow thickness variation [24]) and low initial resistance (LIR) in the range  $50 < R < 200 \Omega$  (thickness 20–40 nm).

The morphological and structural characterization of the cluster-assembled films was carried out by FEG-scanning electron microscopy operating at 5–7 kV of accelerating voltage (SEM model Zeiss Supra 40), and by Cs-corrected transmission electron microscopy, even in high resolution mode. The latter was performed by a ThermoFischer Titan Themis Z microscope operating at 300 kV of accelerating voltage, equipped with an ultra-bright Schottky (X-FEG) electron source, with a double

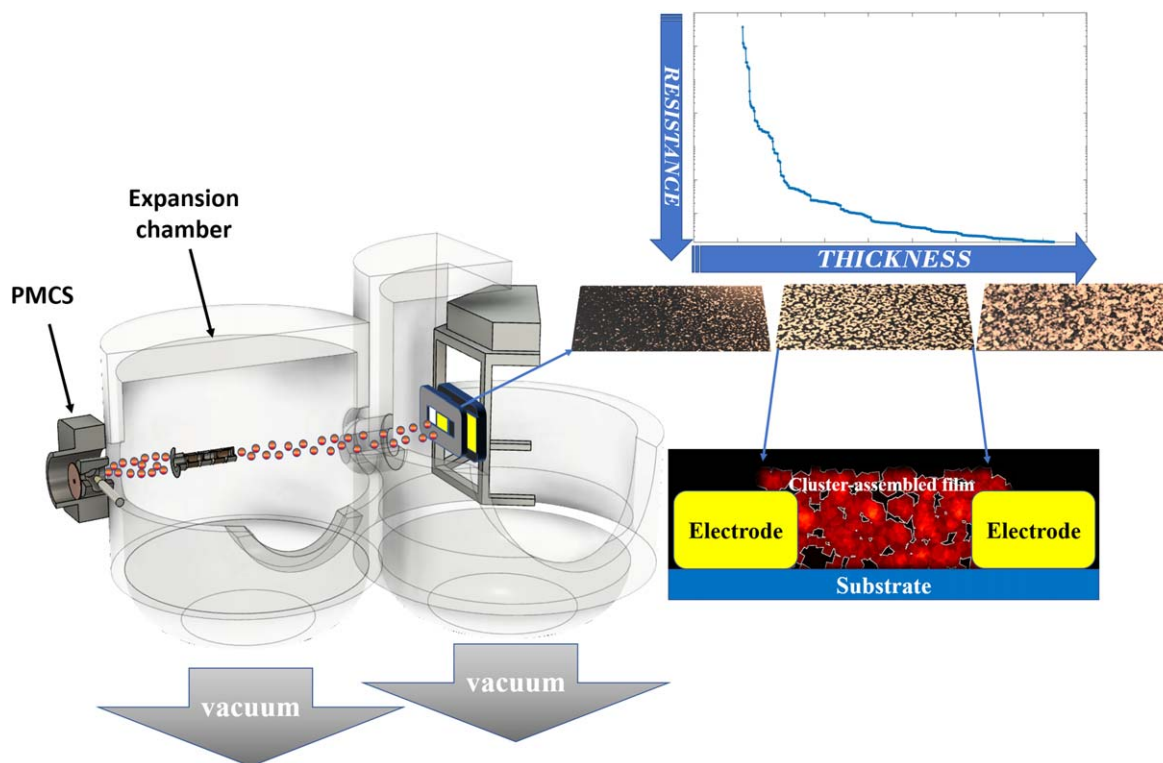


**Figure 1.** Schematic representation of a SCBD apparatus equipped with a PMCS source (not to scale). Au clusters are grown in gas phase through the ablation of a gold target and then carried in the expansion chamber carried by a seeded supersonic beam. After an aerodynamically focusing (the focuser is depicted in the expansion chamber), the cluster beam impinges on masked substrates mounted on a mobile holder. We report an example of a typical electrical percolation curve taken *in situ* during the deposition, with a decreasing resistance and increasing thickness over the time. The different morphological configurations of the samples, corresponding to different regions of the percolation curve. A schematic representation of a cluster-assembled two-terminal device is also shown (cross section view).

spherical aberration corrector, and a 16 MP CMOS Ceta camera. TEM/HRTEM imaging was performed on a thin film (average thickness 12 nm) deposited on an amorphous and thin (10 nm) substrate of silicon nitride.

## 2.2. Electrical characterization

The electrical conduction properties of the devices were tested under two protocols using a High-Power Source Measurement Unit (HPMSU, Agilent E52790A): the application of both train of voltage pulses and of constant voltage over the time. The resistance  $R$  of the devices was obtained through the Ohm law ( $R = \frac{V}{I}$ ) by applying a voltage  $V$  and measuring the current  $I$  in the device. The HPMSU was remotely controlled through a LabVIEW script to synchronize the application of the voltage and the measurement of the current at the desired sampling rate.

In the case of constant applied voltage, the current was sampled every 50 ms for several minutes (20 000 points, equivalent to 1000 s of total application time). When using trains of voltage pulses, to excite the device one pulse was applied lasting 100 ms and 1 s (pulse time width), respectively, and with a voltage amplitude spanning an interval between 3 and 40 V. Then a subsequent train of 8 sensing pulses at 1 V (duration of 50 ms and period of 70 ms) followed the excitation to measure the current and thus to observe the evolution of the resistance.

## 2.3. Data analysis method

We performed a threshold analysis in order to distinguish switching events from random noise. This was obtained by computing the relative difference of consecutive resistance values in the temporal resistance series and setting a threshold to discriminate from noise. Figure 2 shows a pattern of the resistance evolution of a typical cluster-assembled film over the time under a voltage application of 15 V. The threshold value was chosen calculating the standard deviation of an interval without switching events (the blue and red intervals in figure 2, with the respective distribution on the bottom) normalized by the average of the selected values. In this way a switching event is defined as two consecutive resistance values that differ by a number greater than the computed standard deviation:

$$\frac{R_{i+1} - R_i}{R_i} > n * \sigma_{normalized} \quad (1)$$

with  $n = 4$  to obtain a robust thresholding process and to avoid the recognition of spurious events. In the case of random noise, the resistance values should be normally distributed, when the difference between two values is greater than four times the standard deviation, then there is a high probability that a switch occurs.

Data analysis is performed through a software developed in MATLAB environment, which implements the method to recognize the switches, and computes the quantity of interest

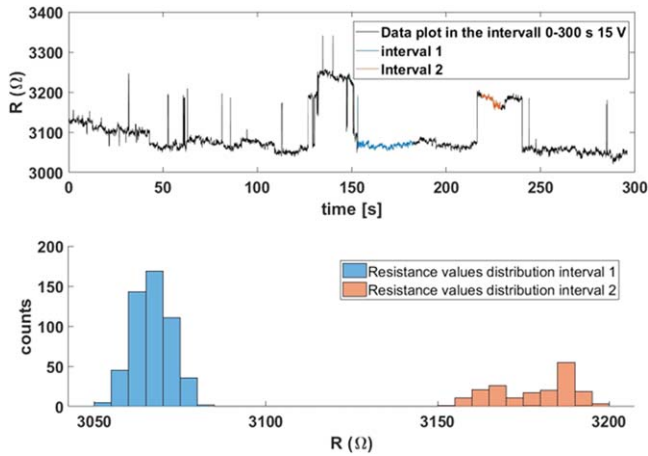


**Figure 2.** Top panel reports the spontaneous activity for the electrical resistance as function of time for a cluster-assembled film under the application 15 V bias. The two selected intervals for the  $\delta\alpha$  computation are shown highlighted in blue and orange. Bottom panel reports the distribution of the resistance values for the two selected intervals shown with the same color code. The first interval has a distribution of the resistance values peaked around 3060  $\Omega$ , while the second one is more broadened, hint of the presence of switch events with low amplitude (less than 100  $\Omega$ ).

in (1) for the whole data series. To compute  $\sigma_{normalized}$ , it is possible to select several intervals where no presence of switches appears, like shown in figure 2, and to observe the resistance value distribution for each interval.

The normalized standard deviation of the data is computed for each selected data interval and stored in memory. The intervals are selected in order to be representative of each explored resistance level, selecting different portions of data resistance values (figure 2). The standard deviation in (1) is chosen evaluating the explored resistance levels during the thresholding process. In this way, the different amplitude of the random noise, for different resistance levels, is taken account, particularly when the switch amplitude is of different orders of magnitude. This allows to analyze large amounts of data and provides an objective method for the switch events identification preventing the presence of artefacts. After the recognition step, the series of switch events is obtained, and it can be treated like a point process in time, a collection of point related to the presence or the absence of the events.

The analysis is carried out for each resistance series measured at different voltage values (5, 15, 25 V). We evaluated the Inter-Switch-Interval (ISI) distribution by computing the temporal distance  $t_{ie} = t_{i+1} - t_i$  (the inter-event time) of consecutive switches for the whole interval. The data are plotted in form of probability density distribution function. To fit the function that describe the distribution we used the maximum likelihood method [23, 35] implemented in MATLAB (see MATLAB documentation at [36]). This approach has the advantage to not be sensitive to the choice of the number of bins for the distribution. We fit both power law and double exponential function and choose the best one comparing the width of confidence bound interval computed for the fit [36].

To further confirm the presence of correlations in sequences of discrete switching events, analysis such as the one proposed by Karsai *et al* in [37] was performed. We counted the number of consecutive switches that falls into a burst period if  $t_{ie} < \Delta t$ , where  $\Delta t$  is a fixed time interval, longer than the inverse of the sampling frequency. We plotted the distribution of the number of events that belong to the same burst period both for the original and for shuffled data, that should show a non-correlated behavior. The distributions for the two cases are compared to evaluate the differences among them in order to identify the degree of randomness in the switch occurrences. Usually an exponential decay in the distribution data tail is expected for independent and uncorrelated events; on the converse, an heavy tail (a deviation from this exponential behavior) should indicate the presence of temporal correlations in the data [8, 37].

### 3. Results and discussion

#### 3.1. Cluster-assembled film structure

Cluster-assembled Au films were characterized by TEM, HRTEM and SEM at different thicknesses. In figure 3 we show the TEM imaging of a typical film at increasing magnification. We performed the characterization on a film with average thickness of 12 nm in order to guarantee both the transmission of the incident electron beam and the observation of the first stage of the film growth. The cluster-assembled film has a structure consisting of branched aggregates based on the hierarchical arrangements of small units in larger features up to a certain critical length-scale, determined by the time of the deposition process [38].

The incident cluster size distribution affects the film growth dynamics: the surface diffusion on the silicon substrate and the nucleation are favored for smaller clusters initially resulting in a 2D growth, while larger clusters act as static nucleation sites where a 3D growth mode is promoted [38, 39]. HRTEM characterization shows that the branched structures and larger aggregates are mainly constituted by several crystal domains that have grown with no preferential direction, as expected for a deposition on an amorphous substrate [40]. Figure 3 clearly displays two most important features belonging to the deposited film: (i) the branched structure does not show any isolated cluster (see panels (a)–(c)), suggesting that the percolation threshold has been largely reached; (ii) the HRTEM image (panel (d)) shows that the islands forming the film are in turn constituted by several crystal domains, with size (calculated as domain wall length) ranging between 5 and 10 nm. Moreover, they are randomly grown and in different possible crystal relationships among them: some of them are twinned domains, while in other cases the domains are just separated by grain boundaries, often with frequent stacking faults, in order to minimize the surfacial interface energy. Finally, in some case a superposition of crystal domains is also observed, and that is easily identifiable by the Moiré fringes' presence.

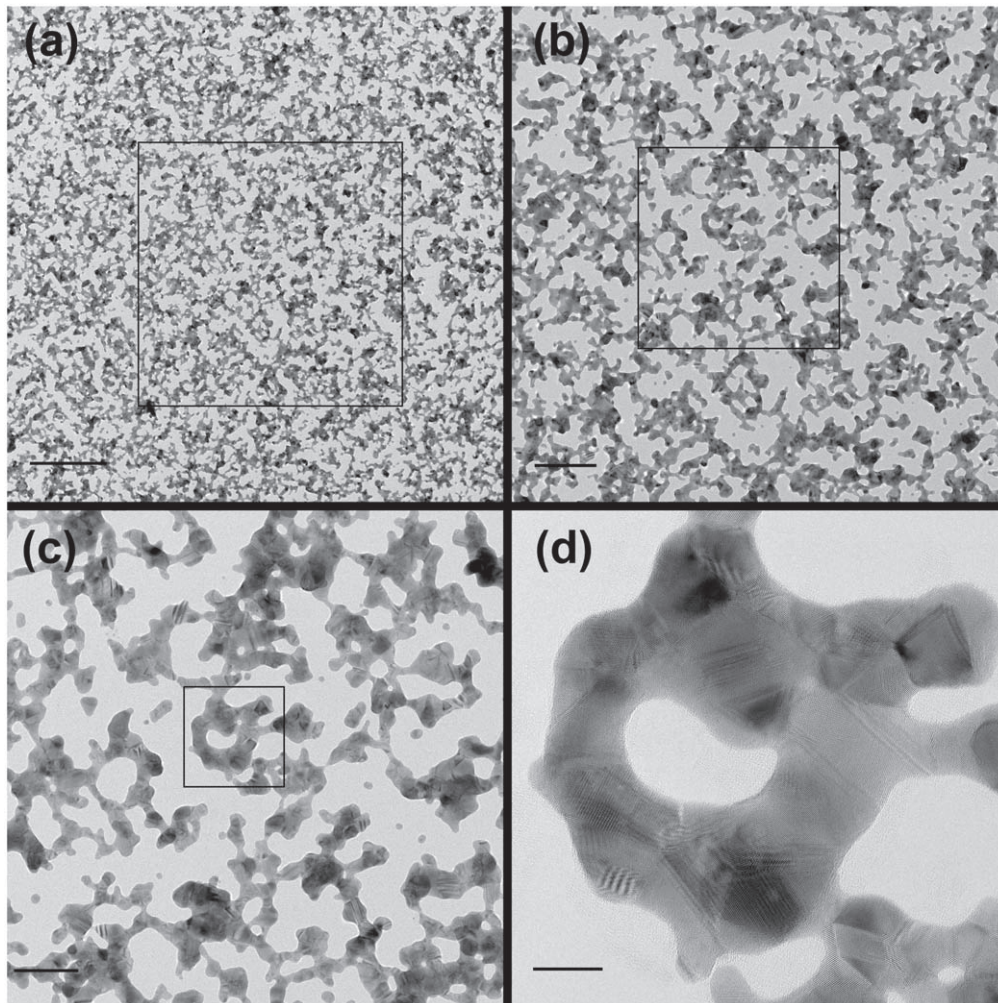


**Figure 3.** TEM/HRTEM images of the gold clusters. (a) Overall view of the percolating film, scale bar: 250 nm; (b) magnified view of the square reported in panel (a), scale bar: 100 nm; (c) magnified view of the square reported in panel (b), scale bar: 50 nm; (d) HRTEM image of the polycrystalline cluster surrounded by the square in panel (c), scale bar: 10 nm.

In general, what is indicated by the HRTEM imaging is that the occurrence of the above-mentioned different possible crystal domains configuration is very likely dictated by the local thickness: if it increases, the structure evolves from quasi 2D crystal domain to twinned ones, to further and finally give rise to their superposition.

The structure of thicker films was also investigated by SEM: figure 4 shows SEM micrographs of typical HIR (figure 4(a)) and LIR (figures 4(b) and (c)) Au films. We observe a complex structure resulting from the random stacking of clusters and characterized by a network of connected islands, gaps, and complex multilinked structures. The SEM characterization of HIR confirms what already observed by TEM. Figure 4(c) taken from a LIR film with a thickness of 57 nm clearly shows a granular structure at the nanoscale resulting from the ballistic deposition growth regime typical of SCBD [38, 40]. HIR films are characterized by a lower number of junctions between large islands and by a 2D organization, whereas the LIR ones are highly interconnected fully and 3D films present cluster aggregates bridged by tiny

junctions and higher density of small isolated island (insets of figures 4(a) and (b)).

Cluster-assembled films fabricated by SCBD are characterized by a hierarchical arrangement of nanoscale building blocks in larger structures producing topography, high specific area, and porosity that can be accurately controlled and varied at the nano- and mesoscale [41, 42]. The process of formation of a nanostructured thin film by SCBD takes place in a ballistic deposition regime [38], hence the deposition time controls the morphology of the films, which evolves regularly according to simple and reproducible scaling laws [38]. The roughening of surfaces and interfaces resulting from the bottom-up assembling of clusters has a fundamental relevance for their functional properties including electrical conduction [43].

### 3.2. Resistive switching and spiking behavior

Nanostructured Au films show a resistive switching activity under the application of a constant or variable voltage [25, 26]. The behavior of two-terminal devices fabricated

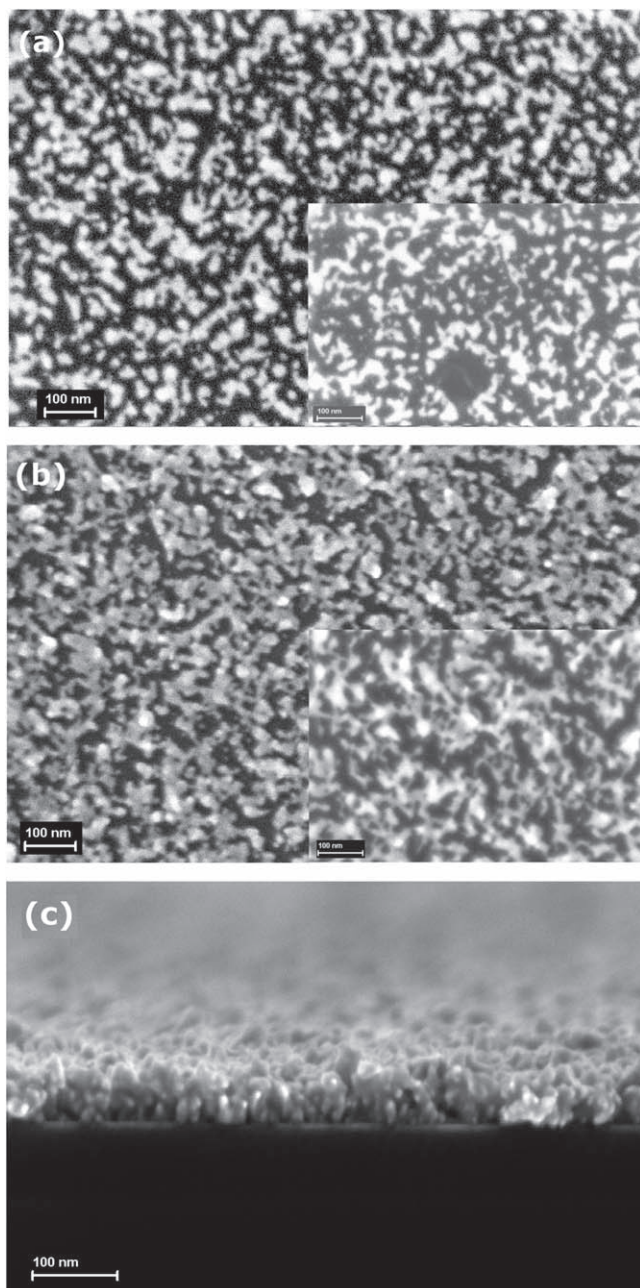


**Figure 4.** (a) Top-view SEM micrograph showing the surface morphology of a HIR cluster-assembled Au film (EHT 5.00 kV). The thickness of the film is 14 nm. The inset shows an enlargement where a poorly connected film characterized by the presence of several isolated structures is visible. (b) Top-view SEM micrograph showing the surface morphology of a LIR cluster-assembled Au film (EHT 5.00 kV). The thickness of the film is 25 nm. The inset shows an enlargement where a fully connected network of cluster is clearly visible. (c) Cross section of a cluster-assembled films 57 nm thick (EHT 7.00 kV). The observed morphology is characterized by nanoscale porosity, poorly connected and non-compact structures with lower density with respect to bulk and increasing surface roughness with film thickness.

with films close to the percolation threshold have been characterized in detail: they show features similar to those reported for other systems based on the assembling of nanoobjects [20, 22, 27].

Recently, we demonstrated that nanostructured Au films with thickness well beyond the percolation threshold show complex resistive switching behavior [24], here we consider two terminal devices fabricated with cluster-assembled films with variable thickness beyond the percolation threshold and hence with different resistances as described in section 2.1. Figure 5 shows the measured resistance series (red dots identify the switching events as described in section 2.3) both for HIR ((a)–(b) panels), and LIR samples ((c)–(d) panels). For HIR films we observe the onset of a resistive switching activity upon the application of low constant voltages (3 V) with no activation phenomena (see figures 5(a), (e), (b)). In the case of LIR films, an activation event takes place at a threshold voltage ranging from 20 to 30 V in order to observe a switching activity [24]) (see figures 5(c) and (d)). HIR devices (figure 5(a)) show a resistive switching pattern with a small number of events uniformly distributed compared to the LIR, where a more pronounced activity with events grouped in bursts is visible (figure 5(c)). These differences tend to disappear at high voltages (15 and 25 V) (see figures 5(b) and (d)). Events with a higher amplitude take place with a low frequency over the time under the application of a constant voltage.

The switching activity can be controlled by using voltage pulses: figure 6 shows the typical resistance switching pattern observed in HIR devices. This class of samples shows reversible switches with the application of pulses with 3 V excitation pulses and a time width of 100 ms. The amplitude of the resistance variations is usually lower than one order of magnitude.

LIR devices need a threshold voltage (being its value dependent on the initial sample resistance) to activate the switching behavior also under the application of a periodic voltage. At voltage pulses lower than the threshold value, the device shows an ohmic behavior; approaching the threshold values the resistance undergoes an increasing trend as shown in figure 7(a). After the application of each excitation pulse, the resistance increases like an integration process in time. In addition, during the measurements through the sense pulses, it shows a sort of relaxation: a similar feature is observed in neural networks and it is described by the leaky integrate-and-fire neuron (see figure 7(a)) [6, 44]. This type of behavior is more clearly visible with 1 s width pulses. In figure 7(b) the activation of switching activity takes place after the application of voltage pulses for a time window of about 100 s. The number of pulses needed to reach the activation step depends by the voltage level, the pulse width and the number of pulses.

In figure 8 the behavior of the LIR device under the application of voltage pulses after the activation, is shown: with 5 V pulses the device changes the resistance from the high to a lower level for almost one order of magnitude (figure 8(a)), while a transition to a higher resistance state under the application of 20 V pulses is observed (figure 8(b)). The switching from high resistance to low resistance levels is reproducible and stable. We observed that the reversible switching behavior can be controlled tuning the pulse width and the height. For higher voltage pulses (beyond the

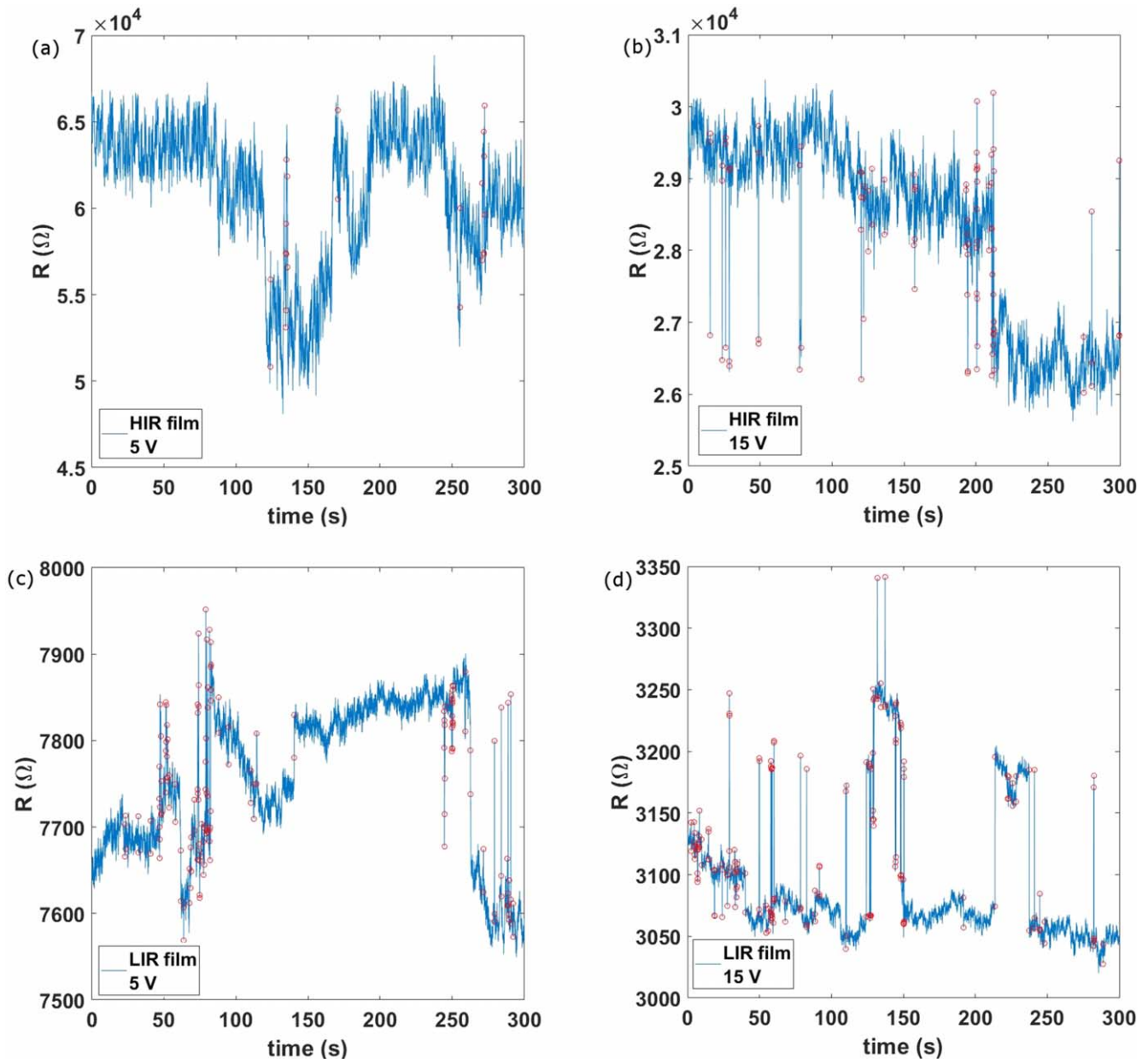


**Figure 5.** Switch activity patterns (in red the events identified as switch) for two different samples under different voltage values in a time window of 300 s. (a) The switching activity for a HIR film under low applied voltage (5 V) characterized by few and uniformly distributed events. (b) Switching activity for the same sample under the application of higher voltage (15 V); the increasing of switching activity is clearly visible. (c) Switching activity for a LIR sample under 5 V and (d) under 15 V. In both cases an intense activity with burst events is visible.

activation level for LIR samples) 100 ms pulses are employed. In figure 8(c) consecutive and reversible switch between higher and lower resistance state are shown with the applied pulses.

As we recently pointed out [24], the observed switching behavior in nanostructured Au films beyond the percolation threshold is quite unexpected and it has never been reported, to the best of our knowledge. In cluster-assembled gold films the granular structure at different length scales largely determines the non-ohmic electrical properties of the system. Although the elemental building blocks can be considered metallic, their assembly does not result in an overall ohmic conductor. The use of ‘good metal’ building

blocks to fabricate ‘bad metal’ systems has been reported in the case of Ag films, assembled with traditional methods, where structural disorder at the mesoscale influenced in a substantial way the electronic properties of the system [45, 46].

In our case, incident clusters form, upon landing on the substrate, larger aggregates without losing their individuality [40, 42]. They physically connect in a continuous network, as shown by SEM and TEM imaging, forming large polycrystalline structures (figure 4) characterized by the presence of a very high density of grain boundaries and stacking faults. These larger polycrystalline structures are loosely connected forming a porous film.



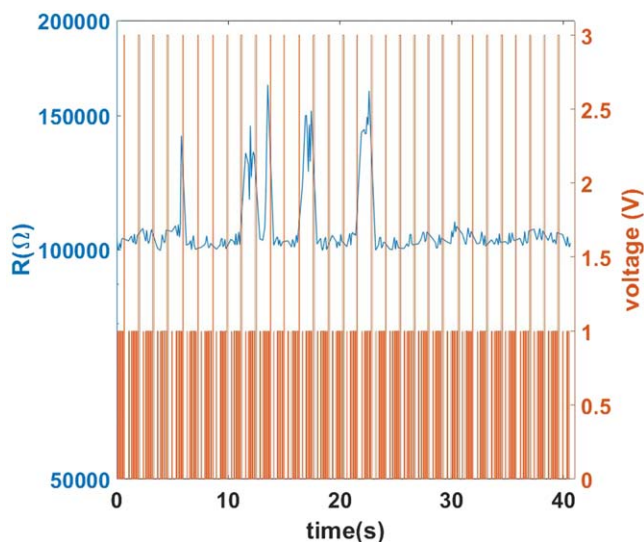


**Figure 6.** Switching activity of a HIR cluster-assembled film under the application of voltage pulses (3 V) (y axis in log scale). Reversible and consecutive events are observed due to the application of low amplitude voltage pulses.

Electronic carrier conduction in these porous systems can be considered to be based of space charge limited conduction mechanisms and coulomb blockade [47] with very strong geometrical constraints [48–50]. The presence of an extremely high density of grain boundaries and crystalline orientation mismatch deeply affect the electrical conduction [45, 51, 52] representing a barrier for the electric charge flow determining and resulting in a distribution of different ‘resistances’ over the cluster-assembled film [53, 54].

The grain boundaries distribution can dynamically change under the current flow because of the formation of local ‘hot spots’ that induce atomic rearrangement, and formation/destruction of contact depending on the power dissipated locally [52–55], as schematically sketched in figure 9. We qualitatively represent in three different steps, the evolution of a grain boundary (different colors indicate different crystalline orientations): the grain boundary region structure depends on the flowing current that determine rearrangements of the crystalline planes resulting in the exploration of different resistance film levels, the transition from configuration 1 to configuration 2 in figure 9 determines the observed switching behavior.

The evolution of the grain boundary structure can be due to Joule heating resulting from current flow through an inter-cluster and intra-cluster (figure 9 sketch 1) [52–55]. The formation of hot spots determines the local rearrangement of the crystalline phases and defect annealing, giving rise to either a further increase of the current (sketch 2) or to a junction break (sketch 3). The modification/breaking of the physical contacts among nanoparticles and the dynamical rearrangement of defects cause the observed resistive switching behavior [23].

In a complex nanoscale junction (see figures 3 and 4), when a point contact between grain is smaller than the mean free path of electron, a small voltage drops (about 100 mV)

can induce high temperature (up to thousands K) [56] causing the re-arrangement of the junction through defect displacement, atom migration and re-crystallization [53, 57].

Starting from this picture one can understand the differences among HIR and LIR samples as arising from the different degree and number of nano- and mesoscale junctions formed during the cluster deposition process. HIR samples are fabricated stopping the deposition close to the percolation thickness where the number of interconnection and junctions is relatively low. The structure is characterized by gaps acting as an effective barrier for the electron flow, thus involving non-ohmic conduction mechanism [58] and bridges, where current can reach high density levels inducing breaking/formation events. This determines the global non ohmic behavior observed since the application of low voltages (figure 6). On the other hand, LIR samples are characterized by a larger number of interconnections between grains with a higher volume density; as a consequence, the dissipated energy for volume unit and current density assume different values compared to those of HIR samples for the same applied voltage. The possibility to observe reversible switches controlled by the voltage pulse amplitude is due to the balance between connections formation and breaking taking place at the nanoscale for the different applied voltage values [23]. Higher voltages cause a higher flowing current inducing several and consecutive breaking phenomena between grains.

### 3.3. Switching correlation structure (ISI)

In order to verify the existence of a degree of correlation among the electrical spikes observed in the cluster-assembled films, we performed the Inter-Switch-Interval distribution analysis as in the case of neuronal networks [8, 23]. In figure 10 we report the ISI distribution for both LIR and HIR devices polarized at 5 V. The distributions show a high number of consecutive switches characterized by small interval time between each other, giving rise to the higher peak in the graphs. The longer time intervals are determined by period of silence, i.e. where no switches are present; they determine the tail at higher time interval in the ISI distribution.

The maximum reached interval value can be different for each class of samples. It is usually higher for LIR samples (like the case in figure 10(a), these results arise from a pattern with bunches of events (bursts) separated by longer interval of times (see figures 5(c) and (d). For HIR samples we observe shorter intervals as shown in figure 10(b), resulting from a pattern of switches more uniformly distributed than the first one (like that shown on figures 5(a) and (b). In both cases we investigated the distribution trend fitting exponential and power laws through the maximum-likelihood method [23, 35], and we compared the confidence bounds of the estimated parameters in both cases. We verified a power law trend (figure 10(a)) for LIR devices; for HIR samples at low applied voltage a bi-exponential trend better fit the data (figure 10(b)). We argue that these differences arise from the different morphological properties and number of junctions.

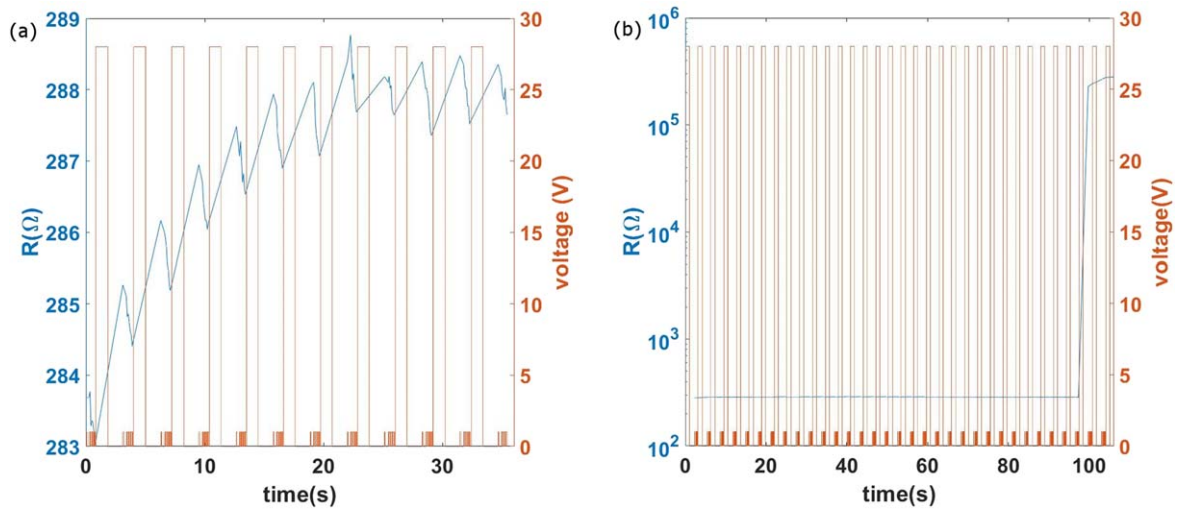


**Figure 7.** (a) Potentiation behavior of LIR samples under the application of a train of pulses near the voltage threshold (27 V in this case, width 1 s). (b) Switching activation of the LIR film (y axis in log-scale). After the potentiation trend shown in (a), the resistance abruptly increases. Note that the resistance scale does not allow to recognize the potentiation progression that appears as a straight line.

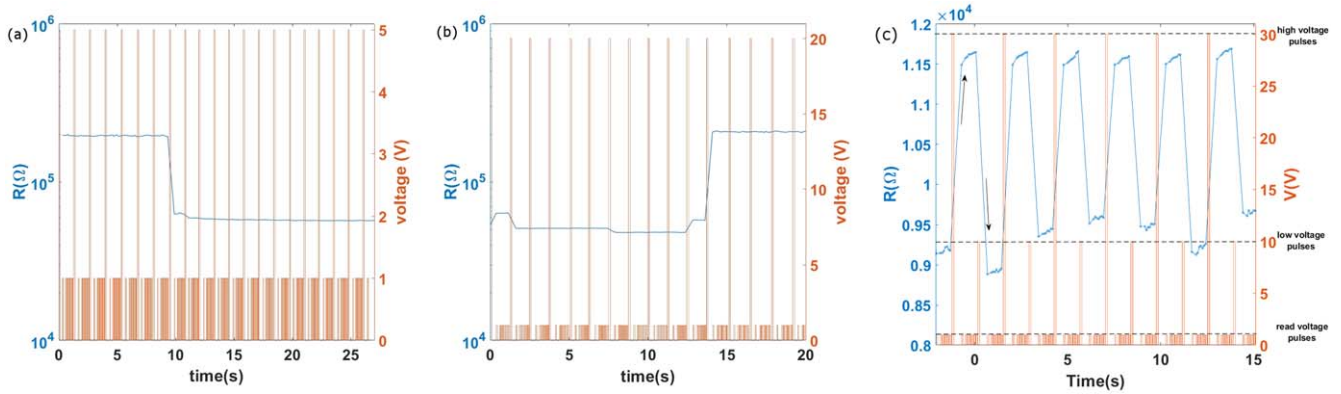


**Figure 8.** (a) Transition to a low resistance level under the application of low voltage pulses (5 V) for LIR sample. (b) Transition to a higher resistance level under the application of high pulses (20 V). Y axis in log-scale for both graphs. (c) An example of consecutive transition from the higher resistance level to the lower one and vice-versa for a LIR sample observed under the application of consecutive low (10 V) and high (30 V) voltage pulses.

For the LIR case, the presence of longer silence period in the resistance series at higher voltages (see figures 5(c)–(d) and the related discussion in the text) imprints a heavier tail to the ISI distribution.

This wide range of explored intervals can originate from the variety of structural defects and the consequent energy and time scale involved in their evolution. As an example, we consider the vacancy diffusion mechanism that could be responsible for the resistance fluctuation, being it capable to cover a wide range of relaxation-time interval, from  $10^{-11}$  to  $10^7$  s [58].

To confirm this behavior, we compare the ISI distribution obtained in different condition in figure 11. The ISI distribution and the fit results for two set of data obtained with two different thresholds ( $n = 4$  and  $n = 6$  in equation (1)). The results clearly show that there is no strong influence on the choice of the threshold in the explored range. The ISI distribution for different samples (both LIR and HIR ones) in figure 11(b) and under different applied voltage (figure 11(c)) confirmed the previous observations: LIR samples present a

higher number of events at higher ISI (see the tail in figure 11(b)), while at higher voltages can trigger an higher number of bursted events (compare the trend of the curves in figure 11(c)). In LIR devices we observe longer ISI, as shown in figure 10(a), because of the presence of a larger number of junctions and connections that require a higher energy dissipation to activate bursts of switches. This makes the events more grouped, with a lower probability (longer intervals between events) but with a high number of events after the activation (avalanche process).

This indicates a correlation between the switching events, as further suggested by the pronounced tail of the ISI graph in log scale.

In order to corroborate this observation, we performed the burst analysis comparing shuffled and original data (as described in the last part of section 2.3). The results are shown in figure 12(a), where the distribution of the bursty period (defined as the sequence of the number  $n$  of events where each one follows the other in a time window  $\Delta t$ ) is plotted for different  $\Delta t$ : the dotted curves (shuffled data) has a faster

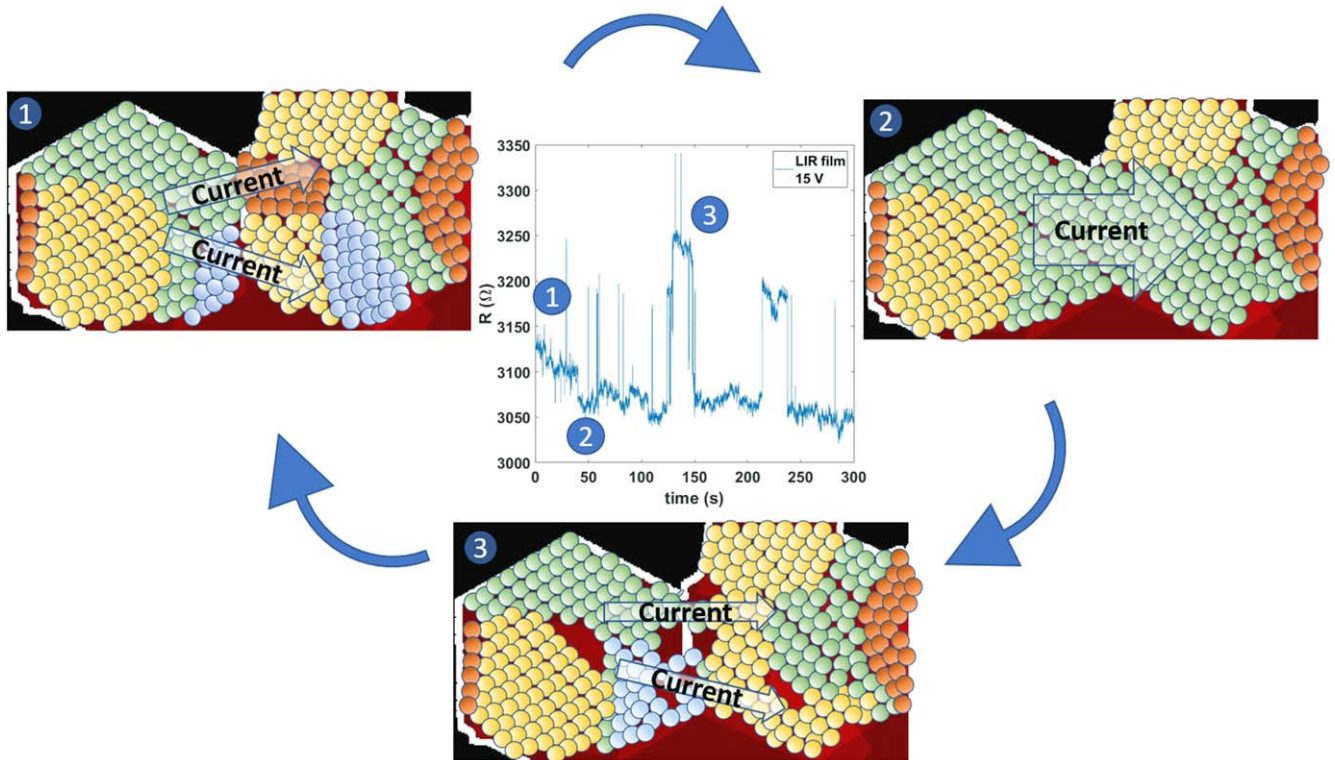


**Figure 9.** Schematic representation of the atomic rearrangements at a single grain boundary, due to current flow, giving origin to switch events. Different colors identify regions with different crystalline orientations. The starting configuration (1) represents the initial grain boundary atomic arrangement. During current flow through the boundary joule heating causes locally a temperature increase that favors crystalline plane rearrangement and defect elimination thus decreasing the local resistance (2). The higher current density causes further heating and breakdown of the electrical connection (3) resulting in a sudden increase of resistance. The current flow redistribution among adjacent regions causes further atom migration and reconstruction of the electrical connectivity between the grains (back to 1). This dynamical rearrangement is at the origin of the spiking behavior reported in the central panel.

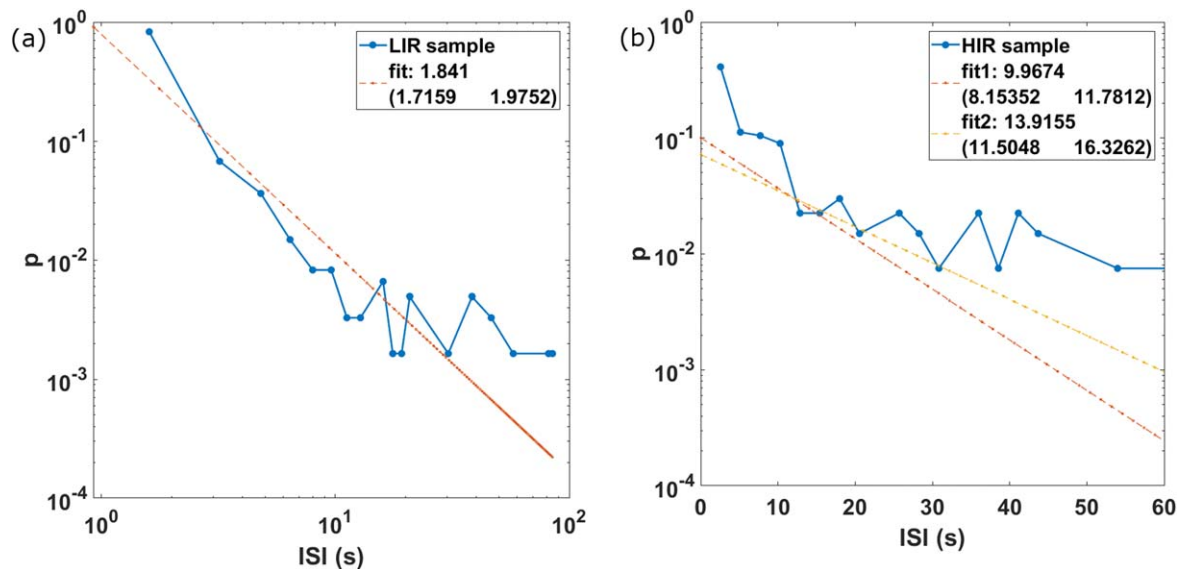


**Figure 10.** ISI distribution for measurements at 5 V. (a) Results for a LIR sample: the power law obtained by the maximum likelihood method is shown in the log-log scale graph (the estimated parameter with the confidence bounds at 95% certainty level is shown in the legend) (b) Results for a HIR sample: the bi-exponential trend that better fit the data are shown in the graph in semi-log scale (the estimated parameter for each exponential branch with the confidence bounds at 95% certainty level is shown in the legend).

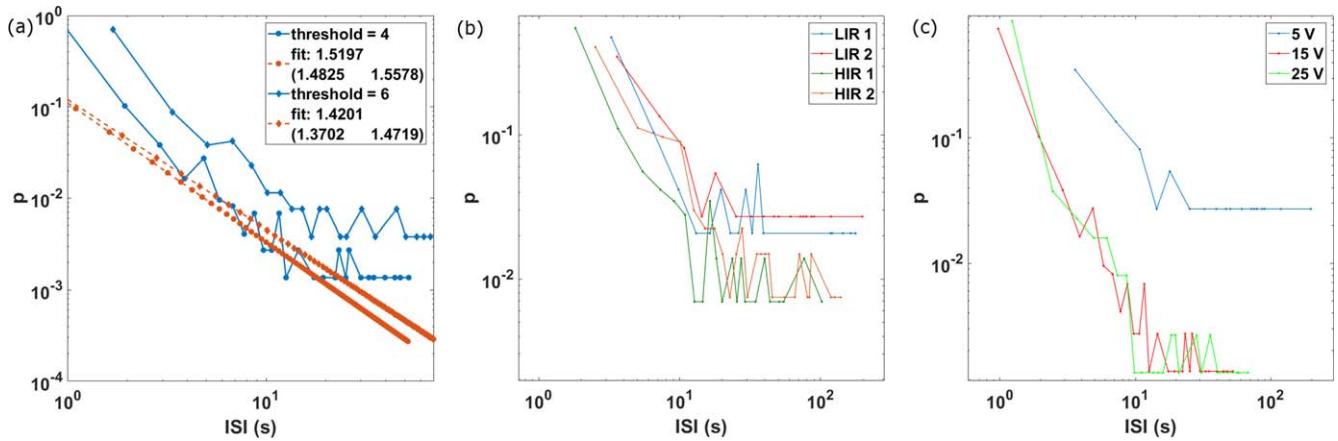


**Figure 11.** (a) ISI distribution for the same sample under the same applied voltage at different threshold. The distribution and the resulting fit are not substantially affected by the chosen threshold. (b) ISI distribution for different samples (LIR samples blue and red curves, HIR samples green and yellow curve) obtained under the same applied voltage (5 V). (c) Typical ISI distributions for one sample obtained under different applied voltage (5, 15, 25 V). This shows as the applied voltage can determine the inter-switch interval distribution.

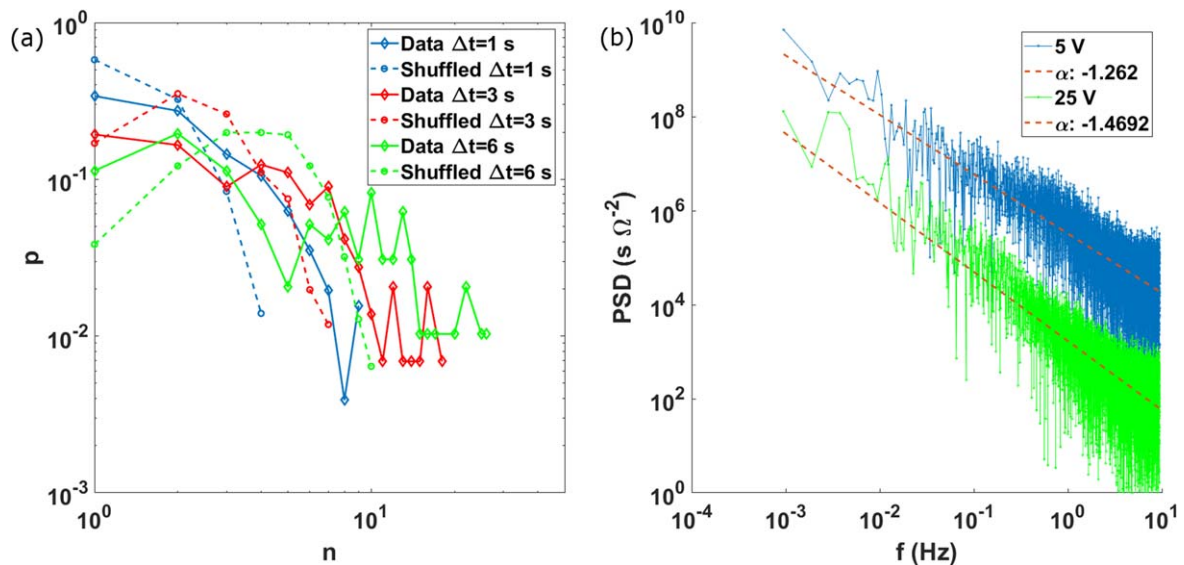


**Figure 12.** (a) The number of consecutive event distribution for different time windows  $\Delta t$  (1, 3 and 6 s) in log scale. Each curve of the number of consecutive events distribution (continuous line) is compared with the distribution obtained after the shuffling process (dotted line). (b) The power spectral density of the resistance data series of a cluster-assembled film in log scale for the same sample under two different applied voltage (5 and 25 V).

decrease than the continuous ones (original data). This is due to the presence of longer ISI in the data that are washed away after the shuffling process. In samples with a more uniform switching pattern (like in HIR samples at low applied voltage) the two curves are more similar (data not shown). Although we cannot fit a power law trend due to the small number of points, a pure exponential behavior (that should be an hint of independent and random events [37]) has never been observed for the original data; we never observed exponential trend for the data and the curve shows a heavy tail unlike the shuffled data one. We point out that similar trend is encountered studying the electrical activity of neurons (see or example [37, 59]). To exclude the influence of the selected time window to perform the analysis, we compared different curves in the same graph (figure 12(a)): they all show the same trend; the slight difference in the green curve can arise

from the higher time window so that uncorrelated periods are merged together.

We also performed the analysis of the power spectral density (PSD) of the overall data noise. The fluctuations in measured electrical quantities can give important information about the phenomena involved in the flowing of charges and their interaction with the particles that compose the studied system [58, 60]; so the PSD can give a deeper insight into their time correlation [61–64]. The measured resistance of cluster-assembled films shows a  $1/f^\alpha$  scaling behavior in the range of analyzed frequencies (figure 12(b)), with  $1 < \alpha < 1.5$ . No significant differences were observed among LIR and HIR devices. We observe a dependence of the exponent  $\alpha$  from the applied voltage, resulting in lower absolute value at lower voltage in most cases, as shown in figure 12(b).

## 4. Conclusions

We have quantitatively characterized the resistive switching and the electrical spiking activity of nanostructured Au two-terminal devices under the action of d.c. and pulsed voltage.

Our data show that the electrical behavior is influenced by the initial resistance of the cluster assembled films and that stable and reproducible features in terms of potentiation and reversible transition from low-resistance to high resistance states are present.

The electrical activity of cluster-assembled films is characterized by irregular bunches of spikes caused by resistive switching events, their analysis in terms of ISI show a strong correlation for bin widths of seconds; burst size and duration follow power law distributions. The spiking dynamics can be described by a power law distribution for LIR devices. The measured resistance of cluster-assembled films shows a  $1/f^\alpha$  scaling behavior in the range of analyzed frequencies.

Au cluster-assembled films have a nanocrystalline structure characterized by an extremely high density of grain boundaries and crystalline orientation mismatch that deeply affects the electrical conduction. The flow of electric current causes the rearrangement of nanocrystalline domains and grain boundaries with the consequent dynamical creation and destruction of pathways with variable resistance causing the switching events.

The simplicity of fabrication and integration of nanostructured Au two-terminal devices on standard and polymeric substrates [26] make them very interesting candidates for the integration of neuromorphic elements in systems where the use of standard CMOS-based technologies is difficult and expensive [65]. The switching activity and its dependence from external stimuli [26] can open interesting perspectives for the fabrication of systems where a certain degree of stochasticity is needed [14, 31] and for the development of memsensing platforms [66].

## Acknowledgements

This work has been supported by Fondazione CARIPLO under project ASSIST (2018-1726), under the Program ‘Call to support the knowledge transfer in advanced materials research’.

## ORCID iDs

A Falqui  <https://orcid.org/0000-0002-1476-7742>

P Milani  <https://orcid.org/0000-0001-9325-4963>

## References

- [1] Rajendran B, Liu Y, Seo J S, Gopalakrishnan K, Chang L, Friedman D J and Ritter M K 2013 Specifications of nanoscale devices and circuits for neuromorphic computational systems *IEEE Trans. Electron Devices* **60** 246–53
- [2] Boybat I *et al* 2018 Neuromorphic computing with multi-memristive synapses *Nat. Commun.* **9** 1–12
- [3] Mead C 1990 Neuromorphic electronic systems *Proc. IEEE* **78** 1629
- [4] Pfeil T *et al* 2013 Six networks on a universal neuromorphic computing substrate *Front Neurosci.* **7** 1–17
- [5] Indiveri G *et al* 2011 Neuromorphic silicon neuron circuits *Front. Neurosci.* **5** 1–23
- [6] Kandel E R, Schwartz J H and Jessell T M 2000 *Principles of Neural Science* (New York: McGraw-Hill)
- [7] Kuzum D, Yu S and Philip Wong H S 2013 Synaptic electronics: materials, devices and applications *Nanotechnology* **24** 382001
- [8] Mazzoni A, Broccard F D, Garcia-Perez E, Bonifazi P, Ruaro M E and Torre V 2007 On the dynamics of the spontaneous activity in neuronal networks *PLoS One* **2** e439
- [9] Izhikevich E M 2003 Simple model of spiking neurons *IEEE Trans. Neural Netw.* **14** 1569–72
- [10] Connors B W, Gutnick M J and Prince D A 1982 Electrophysiological properties of neocortical neurons *in vitro* *J. Neurophysiol.* **48** 1302–20
- [11] Feller M B 1999 Spontaneous correlated activity in developing neural circuits *Neuron* **22** 653
- [12] Lonardoni D, Amin H, Di Marco S, Maccione A, Berdondini L and Nieuws T 2017 Recurrently connected and localized neuronal communities initiate coordinated spontaneous activity in neuronal networks *PLoS Comput. Biol.* **13** 1–27
- [13] Segev R, Benveniste M, Hulata E, Cohen N, Palevski A, Kapon E, Shapira Y and Ben-Jacob E 2002 Long term behavior of lithographically prepared *in vitro* neuronal networks *Phys. Rev. Lett.* **88** 4
- [14] Al-Shedivat M, Naous R, Cauwenberghs G and Salama K N 2015 Memristors empower spiking neurons with stochasticity *IEEE J. Emerging Sel. Top. Circuits Syst.* **5** 242–53
- [15] Maass W 2014 Noise as a resource for computation and learning in networks of spiking neurons *Proc. IEEE* **102** 860–80
- [16] Faisal A A, Selen L P J and Wolpert D M 2008 Noise in the nervous system *Nat. Rev. Neurosci.* **9** 292–303
- [17] Camuñas-Mesa L A, Linares-Barranco B and Serrano-Gotarredona T 2019 Neuromorphic spiking neural networks and their memristor-CMOS hardware implementations *Materials* **12** 2745
- [18] Diederich N, Bartsch T, Kohlstedt H and Ziegler M 2018 A memristive plasticity model of voltage-based STDP suitable for recurrent bidirectional neural networks in the hippocampus *Sci. Rep.* **8** 1–12
- [19] Du C, Cai F, Zidan M A, Ma W, Lee S H and Lu W D 2017 Reservoir computing using dynamic memristors for temporal information processing *Nat. Commun.* **8** 1–10
- [20] Bose S K, Shirai S, Mallinson J B and Brown S A 2019 Synaptic dynamics in complex self-assembled nanoparticle networks *Faraday Discuss.* **213** 471–85
- [21] Stieg A Z, Avizienis A V, Sillins H O, Martin-Olmos C, Aono M and Gimzewski J K 2012 Emergent criticality in complex turing B-type atomic switch networks *Adv. Mater.* **24** 286–93
- [22] Avizienis A V *et al* 2012 Neuromorphic atomic switch networks *PLoS One* **7** 1–8
- [23] Mallinson J B, Shirai S, Acharya S K, Bose S K, Galli E and Brown S A 2019 Avalanches and criticality in self-organized nanoscale networks *Sci. Adv.* **5** 1–8
- [24] Mirigliano M, Borghi F, Podestà A, Antidormi A, Colombo L and Milani P 2019 Non-ohmic behavior and resistive switching of Au cluster-assembled films beyond the percolation threshold *Nanoscale Adv.* **1** 3119–30

- [25] Minnai C, Bellacicca A, Brown S A and Milani P 2017 Facile fabrication of complex networks of memristive devices *Sci. Rep.* **7** 1–8
- [26] Minnai C, Mirigliano M, Brown S A and Milani P 2018 The nanocoherer: an electrically and mechanically resettable resistive switching device based on gold clusters assembled on paper *Nano Futures* **2** 11002
- [27] Manning H G *et al* 2018 Emergence of winner-takes-all connectivity paths in random nanowire networks *Nat. Commun.* **9** 1–9
- [28] Nirmalraj P N *et al* 2012 Manipulating connectivity and electrical conductivity in metallic nanowire networks *Nano Lett.* **12** 5966–71
- [29] De S, Higgins T M, Lyons P E, Doherty E M, Nirmalraj P N, Blau W J, Boland J J and Coleman J N 2009 Silver nanowire networks as flexible, transparent, conducting films: extremely high DC to optical conductivity ratio *ACS Nano* **3** 1767–74
- [30] Yokoyama T, Hirata N, Tsunoyama H, Negishi Y and Nakajima A 2018 Characterization of floating-gate memory device with thiolate-protected gold and gold-palladium nanoclusters *AIP Adv.* **8** 065002
- [31] Buesing L, Bill J, Nessler B and Maass W 2011 Neural dynamics as sampling: a model for stochastic computation in recurrent networks of spiking neurons *PLoS Comput. Biol.* **7** 11
- [32] Wegner K, Piseri P, Tafreshi H V and Milani P 2006 Cluster beam deposition: a tool for nanoscale science and technology *J. Phys. D: Appl. Phys.* **39** R439
- [33] Barborini E, Piseri P and Milani P 1999 Pulsed microplasma source of high intensity supersonic carbon cluster beams *J. Phys. D: Appl. Phys.* **32** L105
- [34] Piseri P, Tafreshi H V and Milani P 2004 Manipulation of nanoparticles in supersonic beams for the production of nanostructured materials *Curr. Opin. Solid State Mater. Sci.* **8** 195–202
- [35] Clauset A, Shalizi C R and Newman M E J 2009 Power-law distributions in empirical data *SIAM Rev.* **51** 661–703
- [36] 2019 *Statistics and Machine Learning Toolbox User's Guide (R2019b)* MathWorks
- [37] Karsai M, Kaski K, Barabási A L and Kertész J 2012 Universal features of correlated bursty behaviour *Sci. Rep.* **2** 397
- [38] Borghi F, Podestà A, Piazzoni C and Milani P 2018 Growth mechanism of cluster-assembled surfaces: from submonolayer to thin-film regime *Phys. Rev. Appl.* **9** 044016
- [39] Jensen P 1999 Growth of nanostructures by cluster deposition: Experiments and simple models *Rev. Mod. Phys.* **71** 1695
- [40] Bardotti L, Prével B, Mélinon P, Perez A, Hou Q and Hou M 2000 Deposition of clusters on Au(111) surfaces: II. Experimental results and comparison with simulations *Phys. Rev. B* **62** 2835–42
- [41] Podestà A *et al* 2009 Cluster-assembled nanostructured titanium oxide films with tailored wettability *J. Phys. Chem. C* **113** 18264–9
- [42] Bisio F *et al* 2009 Optical properties of cluster-assembled nanoporous gold films *Phys. Rev. B* **80** 205428
- [43] Barborini E *et al* 2010 The influence of nanoscale morphology on the resistivity of cluster-assembled nanostructured metallic thin films *New J. Phys.* **12** 073001
- [44] Mehonic A and Kenyon A J 2016 Emulating the electrical activity of the neuron using a silicon oxide RRAM cell *Front. Neurosci.* **10** 57
- [45] Arnason S B, Herschfeld S P and Hebard A F 1998 Bad metals made with good-metal components *Phys. Rev. Lett.* **81** 3936
- [46] Hebard A F and Arnason S B 1999 Bad-metal behavior: exotic physics or a consequence of microstructure? *J. Supercond.* **12** 159–62
- [47] Acha C 2017 Graphical analysis of current-voltage characteristics in memristive interfaces *J. Appl. Phys.* **121** 134502
- [48] Burr T, Seraphin A, Werwa E and Kolenbrander K 1997 Carrier transport in thin films of silicon nanoparticles *Phys. Rev. B* **56** 4818–24
- [49] Yajadda M M A, Müller K H and Ostrikov K 2011 Effect of coulomb blockade, gold resistance, and thermal expansion on the electrical resistance of ultrathin gold films *Phys. Rev. B* **84** 1–8
- [50] Chen W, Ahmed H and Nakazoto K 1995 Coulomb blockade at 77 K in nanoscale metallic islands in a lateral nanostructure *Appl. Phys. Lett.* **66** 3383
- [51] Steinhögl W, Schindler G, Steinlesberger G, Traving M and Engelhardt M 2005 Comprehensive study of the resistivity of copper wires with lateral dimensions of 100 nm and smaller *J. Appl. Phys.* **97** 023706
- [52] Aguilar M, Oliva A I and Quintana P 1998 The effect of electrical current (DC) on gold thin films *Surf. Sci.* **409** 501–11
- [53] Durkan C and Welland M 2000 Size effects in the electrical resistivity of polycrystalline nanowires *Phys. Rev. B* **61** 14215
- [54] Durkan C, Schneider M A and Welland M E 1999 Analysis of failure mechanisms in electrically stressed Au nanowires *J. Appl. Phys.* **86** 1280
- [55] Johnson S L, Sundararajan A, Hunley D P and Strachan D R 2010 Memristive switching of single-component metallic nanowires *Nanotechnology* **21** 125204
- [56] Halbritter A *et al* 2002 Connective neck evolution and conductance steps in hot point contacts *Phys. Rev. B* **65** 454131–8
- [57] Durkan C and Welland M E 2000 Analysis of failure mechanisms in electrically stressed gold nanowires *Ultramicroscopy* **82** 125–33
- [58] Zhigal'skii G P and Jones B K 2003 *The Physical Properties of Thin Metal Films* (London: Taylor and Francis)
- [59] Bédard C, Kröger H and Destexhe A 2006 Does the 1/f frequency scaling of brain signals reflect self-organized critical states? *Phys. Rev. Lett.* **97** 1–4
- [60] Dagge K, Frank W, Seeger A and Stoll H 1996 1/f noise as an early indicator of electromigration damage in thin metal films *Appl. Phys. Lett.* **68** 1198–200
- [61] Sillin H O *et al* 2013 A theoretical and experimental study of neuromorphic atomic switch networks for reservoir computing *Nanotechnology* **24** 1
- [62] Bak P and Paczuski M 1995 Complexity, contingency, and criticality *Proc. Natl Acad. Sci. USA* **92** 6689–96
- [63] Bak P, Tang C and Wiesenfeld K 1987 Self-organized criticality: an explanation of 1/f noise *Phys. Rev. Lett.* **59** 381
- [64] Sethna J P, Dahmen K A and Myers C R 2001 Crackling noise *Nature* **410** 242–50
- [65] Soni M and Dahiya R 2020 Soft eSkin: distributed touch sensing with harmonized energy and computing *Phil. Trans. A* **378** 20190156
- [66] Vahl A, Carstensen J, Kaps S, Lupan O, Strunskus T, Adelung R and Faupel F 2019 Concept and modelling of memsensors as two terminal devices with enhanced capabilities in neuromorphic engineering *Sci. Rep.* **9** 1–9